Controllable Highly Oriented Skyrmion Track Array in Bulk Fe_3GaTe_2

Yunhao Wang,[1,2,*] Shiyu Zhu,[1,2,*,†] Chensong Hua,[3,*] Guojing Hu,[1] Linxuan Li,[2] Senhao Lv,[1] Jianfeng Guo,[1] Jiawei Hu,[1,2] Runnong Zhou,[1,2] Zizhao Gong,[1] Chengmin Shen,[1,2] Zhihai Cheng,[4] Jinan Shi,[2] Wu Zhou,[2] Haitao Yang,[1,2] Weichao Yu,[3,‡] Jiang Xiao,[3] and Hong-Jun Gao[1,2,5,§]

[1]*Beijing National Center for Condensed Matter Physics and Institute of Physics, Chinese Academy of Sciences, Beijing 100190, China*
[2]*School of Physical Sciences, University of Chinese Academy of Sciences, Beijing 100190, China*
[3]*Department of Physics and State Key Laboratory of Surface Physics, Fudan University, Shanghai 200433, China*
[4]*Department of Physics and Beijing Key Laboratory of Optoelectronic Functional Materials and Micro-nano Devices, Renmin University of China, Beijing 100872, China*
[5]*Hefei National Laboratory, Hefei, Anhui 230088, China*

(Received 14 November 2024; revised 12 February 2025; accepted 17 March 2025; published 28 April 2025)

Magnetic skyrmions are emerging as promising candidates for next-generation information technologies, while the realization of scalable skyrmion lattices with tailored configurations is essential for advancing fundamental skyrmion physics and developing future applications. Here we achieved the controllable generation and regulation of a large-area, highly oriented skyrmion track array (STA) in ferromagnet Fe_3GaTe_2 using a vector-magnetic-field manipulation technique. The orientation and ordering of STA, along with the types and density of skyrmions, are precisely controlled by modulating parameters during the manipulation. The critical roles of in-plane magnetic fields and Dzyaloshinskii-Moriya interaction in STA generation is further confirmed by micromagnetic simulation. Our findings develop a strategy for engineering large-area and highly oriented skyrmion configurations, offering a new pathway for the future application of next-generation spintronic and information technologies.

DOI: 10.1103/PhysRevX.15.021032 Subject Areas: Magnetism

I. INTRODUCTION

Magnetic skyrmions, the topologically protected swirling spin structures, are considered promising candidates for energy-efficient nanoscale memory and logic devices [1]. The observation of skyrmions has been reported across various platforms including bulk chiral magnet crystals [2–5], exfoliated thin flakes [6], interfacially asymmetric magnetic multilayers [7–10], and nanowires [11,12]. Recently, magnetic van der Waals (vdW) crystals have emerged as a new arena for exploring novel magnetic properties and hold significant potential for ultracompact spintronic devices, owing to their easy exfoliation process and capability to maintain long-range ferromagnetic order down to atomic layers or thin flakes [6,13,14]. Specifically, strong perpendicular magnetic anisotropy (PMA), dipolar interaction, Dzyaloshinskii-Moriya interaction (DMI), and skyrmion lattices have been reported in an above-room-temperature vdW ferromagnet Fe_3GaTe_2 [15–23], providing a new platform for manipulating and constructing skyrmion-based configurations.

Currently, skyrmions are commonly reported to be generated from labyrinthine or stripe domains under a perpendicular magnetic field [10,24,25], while the generation on certain materials has also been reported using various other stimuli such as currents [7], laser [26], x-ray [27], electron beam [28,29], and spin-polarized tunneling current [30]. These techniques typically result in either a pure skyrmion phase or a hybrid phase comprising skyrmions interspersed with disordered labyrinthine domains. Recently, advancements have demonstrated current-driven skyrmion motion in devices [31–33], stripe domains [34], and domain walls [35], underscoring the significance of configurations that confine skyrmion chains into one-dimensional structures. Accordingly, developing innovative strategies to design and fabricate ordered magnetic structures that integrate skyrmion chains into well-defined racetracks has emerged as a pivotal research objective for both fundamental studies and potential applications.

*These authors contributed equally to this work.
†Contact author: syzhu@iphy.ac.cn
‡Contact author: wcyu@fudan.edu.cn
§Contact author: hjgao@iphy.ac.cn

Here we report the generation and regulation of a large-area, highly oriented skyrmion track array (STA) in ferromagnet Fe_3GaTe_2 achieved through a vector-magnetic-field modulation strategy. The highly oriented STAs are observed extending across hundreds of micrometers, as revealed by magnetic force microscopy (MFM). It has been confirmed that the orientation, ordering, and skyrmion density of the STA are rigorously controlled by the vector magnetic field in our strategy. Additionally, two types of skyrmions with distinct characteristics and magnetic evolution paths have been controllably generated within the STA. We demonstrate that the underlying mechanism for the formation of the STA is highly dependent on the shrinking propagation period of stripe domains induced by a varying in-plane magnetic field, as supported by micromagnetic simulation.

II. HIGHLY ORIENTED SKYRMION TRACK ARRAY ON Fe_3GaTe_2

Fe_3GaTe_2 is a vdW ferromagnet with each layer consisting of an Fe/FeGa/Fe heterometallic slab enclosed between two Te layers [Fig. 1(a)]. Single crystals of Fe_3GaTe_2 are grown using the chemical vapor transport method, and their high quality is validated by various characterization techniques [Figs. S1(a)–S1(f) in Supplemental Material [36]] including x-ray diffraction, energy-dispersive x-ray spectroscopy, and aberration-corrected scanning-transmission-electron microscopy. Magnetization measurements reveal a high Curie temperature (T_c) at approximately 356 K and a saturation field of around 0.6 T along the c axis [Figs. S1(g)–S1(i) in Supplemental Material [36]]. The strong PMA of Fe_3GaTe_2 crystal is verified by the unsaturated M-H curve in the a-b plane high magnetic field up to 5 T.

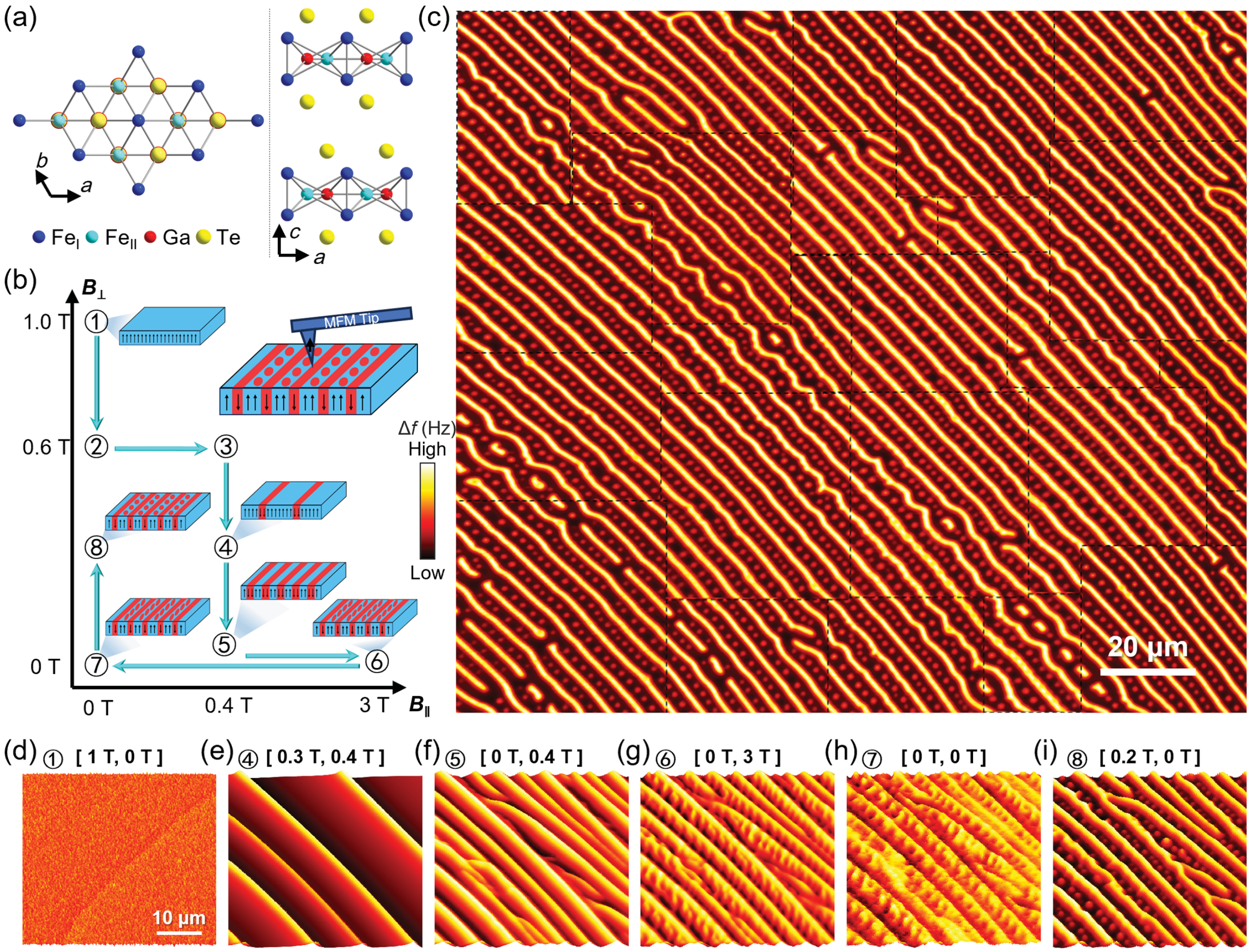

FIG. 1. Highly oriented STA on Fe_3GaTe_2. (a) Crystal structure of Fe_3GaTe_2. (b) Schematic illustrating the generation of a highly oriented STA using a vector-magnetic-field strategy. Inset: schematic of MFM measurements. (c) A stitched large-area MFM image of ordered STA ($166 \times 147\ \mu m^2$) in step 8 ($\boldsymbol{B}_\perp = 0.3$ T, $\boldsymbol{B}_\parallel = 0$ T). In-plane magnetic field $\boldsymbol{B}_\parallel{}'$ hosts an in-plane direction of $\boldsymbol{\theta}_{\mathbf{xy}} = 45°$ in this case. (d)–(i) MFM images unveiling magnetic domain evolution in the formation of STA, which correspond to different steps of the magnetic-field manipulation procedure in (b). The specific step and magnetic-field conditions $[\boldsymbol{B}_\perp, \boldsymbol{B}_\parallel]$ for each image are indicated.

The initial magnetism of Fe_3GaTe_2 cooled from room temperature to 4 K without an external magnetic field is characterized by MFM measurements. These measurements reveal smooth but disordered labyrinthine domains interspersed with a few skyrmions distributed dispersedly among them (see Fig. S2 in Supplemental Material [36]). As the out-of-plane magnetic field ($\boldsymbol{B}_\perp, \boldsymbol{B}_\mathbf{z}$) increases, the labyrinthine domains and skyrmions gradually shrink and ultimately vanish at $\boldsymbol{B}_\perp \approx 0.6$ T, which aligns well with the saturation field observed in the M-H measurement results. By contrast, fewer skyrmions are observed among the labyrinthine domains when magnetic field is decreased back to zero.

To enhance the ordering and density of skyrmions, we have successfully engineered a highly oriented STA using a vector-magnetic-field strategy [see Fig. 1(b) and Video S1 in Supplemental Material [36]]. This macromanipulation technique enables uniform and precise control over the orientation, ordering, and density of the STA across the entire sample, extending over several millimeters. The high-density skyrmion lattice regulated by the highly oriented stripe domains is separated into aligned skyrmion chains on the Fe_3GaTe_2 surface, as demonstrated in an area exceeding $166 \times 147\ \mu m^2$ [Fig. 1(c)].

In this vector-magnetic-field strategy, the magnetic configuration is initially reset using an out-of-plane magnetic field $\boldsymbol{B}_\perp$ exceeding the saturation field (such as $\boldsymbol{B}_\perp = 1.0$ T in our demonstration) [Fig. 1(d), step 1]. Subsequently, $\boldsymbol{B}_\perp$ is reduced to 0.6 T (step 2), which remains well above the thresholds for labyrinthine domain emergence in sample 1 ($\boldsymbol{B}_\perp = 0.20$ T, as shown in Fig. S2 of Supplemental Material [36]) and sample 2 ($\boldsymbol{B}_\perp = 0.35$ T, as shown in Fig. S3 of Supplemental Material [36]). Under the strong magnetic field $\boldsymbol{B}_\perp$ (steps 1 and 2), Fe_3GaTe_2 bulk maintains a saturated magnetization state, with the magnetization $\boldsymbol{m}$ fully pointing along the field direction. As $\boldsymbol{B}_\perp$ is gradually decreased (steps 3–5), the magnetic moment in some regions begins to reverse, forming magnetic domains as the total magnetization decreases, which is confirmed by the evolution of normalized magnetization throughout the process [Fig. S4(c) in Supplemental Material [36]]. Meanwhile, the applied in-plane magnetic field $\boldsymbol{B}_\parallel$ facilitates the transformation of these emerging domains into well-aligned, highly oriented stripes [Figs. 1(e) and 1(f)]. Increasing the in-plane magnetic field to $\boldsymbol{B}_\parallel{}^* = 3.0$ T then generates fragmented structures between adjacent stripes [Fig. 1(g), step 6], which remain stable when the field is decreased to zero [Fig. 1(h), step 7]. The mechanism underlying this novel phenomenon will be discussed in detail in the following text. These fragmented structures between the stripes further evolve into smooth skyrmion chains arranged alternately with stripes, upon the reapplication of an out-of-plane field [Fig. 1(I), step 8]. Further detailed information on the magnetic domain evolution can be found in Supplemental Material Figs. S4 and S5 [36].

We also examined the magnetic stability of the highly oriented STA by reducing the magnetic field to zero and subsequently transferring Fe_3GaTe_2 crystal into an atmospheric environment at room temperature. The precisely controlled characteristics of the highly oriented STA remained stable, as demonstrated over an area exceeding $80 \times 100\ \mu m^2$ (Fig. S6 in Supplemental Material [36]), highlighting its potential applicability in skyrmion-based spintronic devices.

III. REGULATION OF STA VIA VECTOR MAGNETIC FIELD

The orientation of the STA is easily regulated by adjusting the directions of in-plane magnetic field. We performed a series of vector-magnetic-field manipulations during the formation process of stripe domains (steps 3–5), varying the direction ($\boldsymbol{\theta}_\mathbf{xy}$) of the in-plane magnetic field $\boldsymbol{B}_\parallel{}'$ with its strength fixed at 0.4 T. In step 3, the applied $\boldsymbol{B}_\parallel{}'$ induces an integral canting of magnetic moment toward its direction. Since the out-of-plane component of magnetization remains saturated and spatially uniform, no signal contrast appears in MFM images. When $\boldsymbol{B}_\perp$ decreases below the saturation field, uniformed magnetization breaks down as the total magnetization decreases, resulting in the appearance of magnetic domains in the MFM images. To regulate the domain direction, MFM measurements were captured with $\boldsymbol{B}_\perp$ set to 0.2 T and $\boldsymbol{B}_\parallel{}'$ held constant at 0.4 T, while the in-plane direction was altered [Fig. 2(a)]. The stripe domains exhibit a highly adjustable and precisely controllable orientation, consistently aligning perpendicular to $\boldsymbol{B}_\parallel{}'$, indicating the presence of Bloch-type magnetic structures. The Bloch-type domain structure is supported by the orientation of simulated stripe domains, which shows a perpendicular direction with $\boldsymbol{B}_\parallel$ for the Bloch type and a parallel direction with $\boldsymbol{B}_\parallel$ for the Néel type (Fig. S7 in Supplemental Material [36]). The propagation direction of the stripes ($\boldsymbol{\theta}_\mathbf{s}$) and the ordering of the stripe domains were further analyzed using fast-Fourier-transform (FFT) results [Fig. 2(b)], which demonstrate excellent alignment with the in-plane field direction $\boldsymbol{\theta}_\mathbf{xy}$.

This orientation regulation also applies to skyrmion chains. A series of measurements of the final STA structure (step 8) reveal that the skyrmion chains are always aligned and sandwiched between the preconstructed stripe domains [Fig. 2(c)]. The FFT results confirm the alignment of the skyrmion chains, showing a more regular FFT pattern with intensity concentrated around two points, which indicates more uniform spacing between the stripes compared to the pure stripe phase (step 4) [Fig. 2(d)].

The alignment and ordering of the stripes and skyrmion chains are quantified through directional statistics derived from FFT results. Both the integrated intensity (I_FFT, red dots) and the shape parameter (S_FFT, blue dots) are plotted as functions of the in-plane direction $\boldsymbol{\theta}$ [Figs. 2(e) and 2(f)].

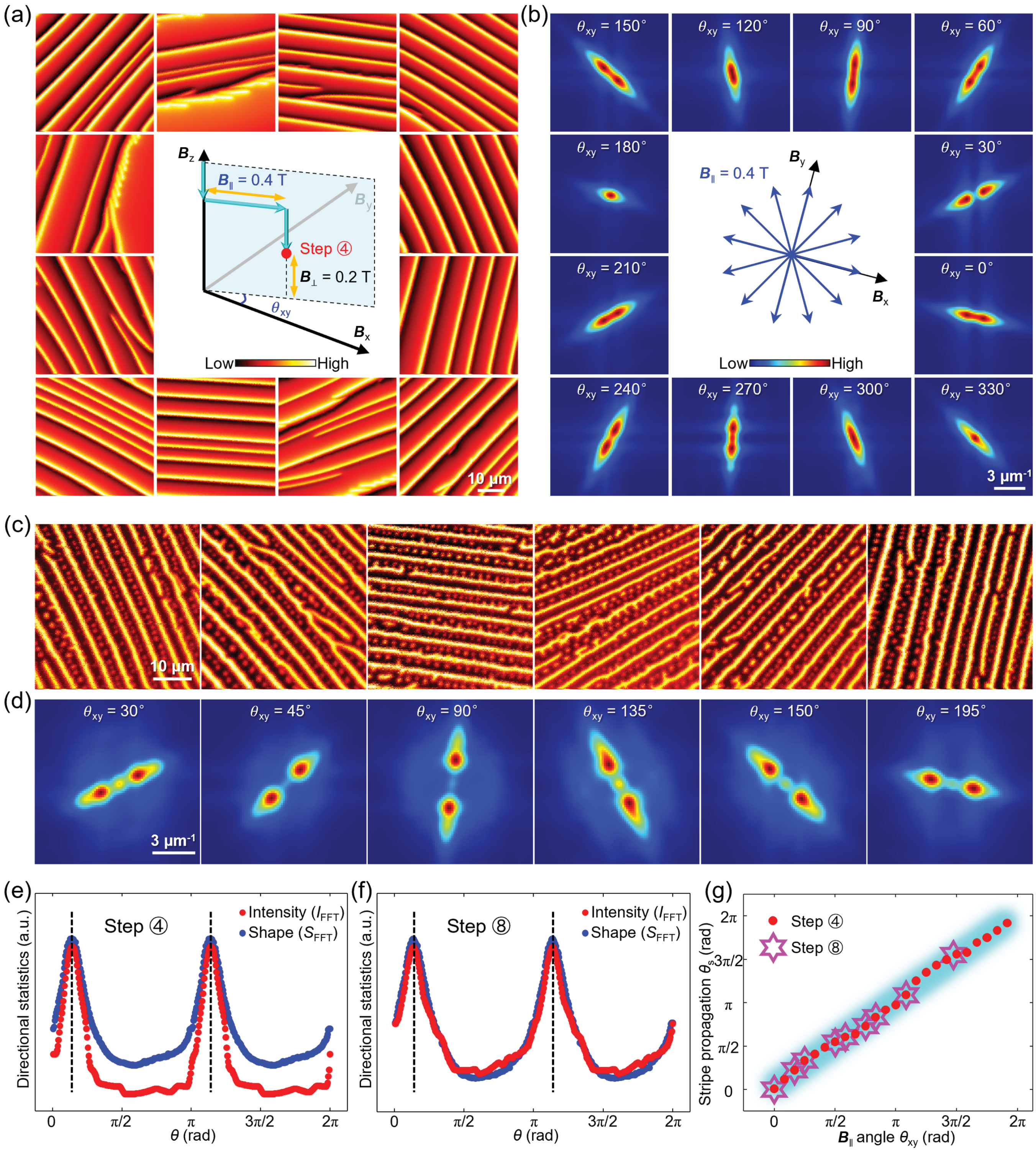

FIG. 2. Regulation of STA orientation by vector magnetic field. (a) Stripe domains in step 4 ($\boldsymbol{B}_\perp = 0.2$ T, $\boldsymbol{B}_\parallel = 0.4$ T) regulated by varying direction of in-plane magnetic field. Inset: a schematic illustrating the vector-magnetic-field manipulation procedure, where the angle $\boldsymbol{\theta}_{\mathbf{xy}}$ varies across different procedures, steps by $\pi/6$ from 0 to 2π. (b) FFT results of MFM images in (a). (c) Highly oriented STA in step 8 ($\boldsymbol{B}_\perp = 0.2$ T, $\boldsymbol{B}_\parallel = 0$ T) regulated by varying direction of in-plane magnetic field, with the $\boldsymbol{\theta}_{\mathbf{xy}} = 30°$, 45°, 90°, 135°, 150°, and 195°. (d) FFT results of MFM images in (c). (e),(f) An example summarizing the variation of I_{FFT} and S_{FFT} with $\boldsymbol{\theta}$ in the FFT results, at $\boldsymbol{\theta}_{\mathbf{xy}} = 30°$ during steps 4 and 8. Both data display consistent peak characteristics, with the peak position indicating the propagation direction of the stripes ($\boldsymbol{\theta}_{\mathbf{s}}$). (g) Variation of the extracted peak position as a function of the in-plane magnetic-field direction $\boldsymbol{\theta}_{\mathbf{xy}}$. The values extracted from I_{FFT} are shown as representatives, with the $\boldsymbol{\theta}_{\mathbf{s}}$ values for stripes in step 4 marked by red dots and those for the STA in step 8 marked by purple hexagonal stars. The shadow area indicates the trend of the linear relationship.

The integrated intensity I_{FFT} is calculated by integrating the intensity from the Γ point to a suitable length that encompasses the main features of the FFT image at a specific in-plane direction $\boldsymbol{\theta}$. The shape parameter S_{FFT} is determined as the distance from the Γ point to the edge at a given $\boldsymbol{\theta}$, using a two-dimensional differentiation method. Both the integrated intensity curves and shape parameter curves exhibit clear and consistent peak characteristics with a periodicity of π at both aligned stripe phase (step 4) and STA phase (step 8), providing a quantified view of the stripe propagation direction $\boldsymbol{\theta}_{\mathbf{s}}$ in each procedures. The strong linear relationship between the in-plane field direction $\boldsymbol{\theta}_{\mathbf{xy}}$ and the stripe propagation direction $\boldsymbol{\theta}_{\mathbf{s}}$ reveals the ability to precisely and continuously manipulate the STA direction [Fig. 2(g)]. Detailed information on orientation regulation is available in the complete MFM images and corresponding FFT images in Supplemental Material Figs. S8 and S9 [36].

The ordering of stripe domains is visibly dependent on, and can be effectively controlled by, the value of the in-plane field $\boldsymbol{B}_{\parallel}'$. We demonstrate this dependence by varying $\boldsymbol{B}_{\parallel}'$ from 0 T (red) to 0.2 T (purple), 0.45 T (blue), and 1.0 T (green), applying these values in step 3 and assessing their effects in the stripe phase (step 4) and STA phase (step 8) [Fig. 3(a)]. In the independent vector-magnetic-field manipulation process with varying $\boldsymbol{B}_{\parallel}'$, the stripe domains

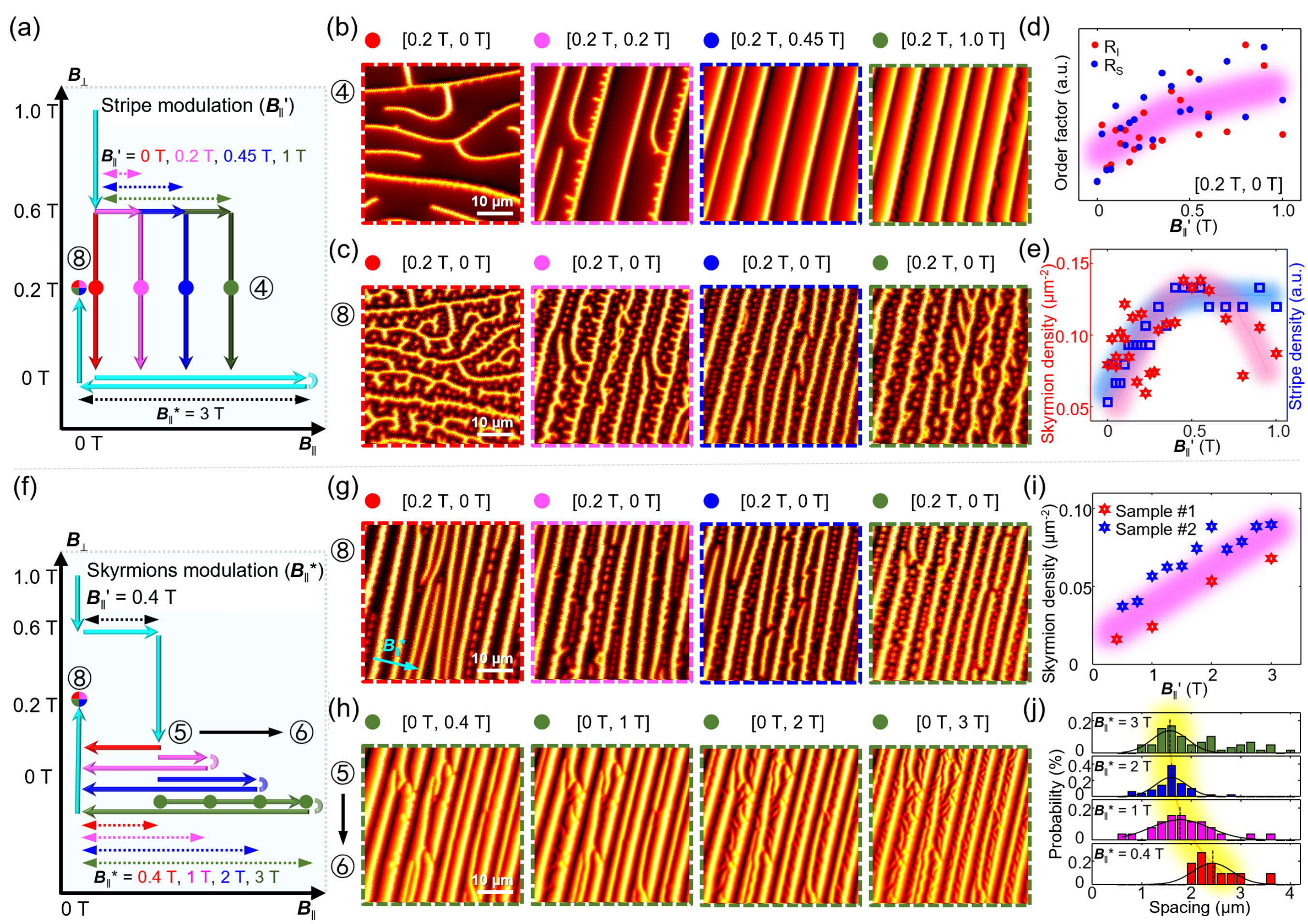

FIG. 3. Modulation of STA ordering and skyrmion density. (a) Schematics of ordering modulation for stripe domains in step 4 and STA in step 8 with varying $\boldsymbol{B}_{\parallel}'$. (b) Labyrinthine and stripe domains induced in step 4 by variable $\boldsymbol{B}_{\parallel}'$. (c) Sequent STA induced in step 8. (d) Variation of stripe order factors extracted in step 8 ($\boldsymbol{B}_{\perp} = 0.2$ T, $\boldsymbol{B}_{\parallel} = 0$ T) tuned by increasing $\boldsymbol{B}_{\parallel}'$, $\boldsymbol{\theta}_{\mathbf{xy}} = 0°$. (e) Variation of stripe density (blue squares) in step 5 ($\boldsymbol{B}_{\perp} = 0.2$ T, $\boldsymbol{B}_{\parallel} = \boldsymbol{B}_{\parallel}'$) and skyrmion density (red hexagonal stars) in step 8 ($\boldsymbol{B}_{\perp} = 0.2$ T, $\boldsymbol{B}_{\parallel} = 0$ T) under increasing $\boldsymbol{B}_{\parallel}'$, $\boldsymbol{\theta}_{\mathbf{xy}} = 0°$. (f) Schematics of modulation of skyrmion density with $\boldsymbol{B}_{\parallel}^*$. (g) STA with rising skyrmion density under increasing value of $\boldsymbol{B}_{\parallel}^*$. (h) Magnetic domain evolution from step 5 to step 6, with $\boldsymbol{B}_{\parallel}$ increasing from 0.4 to 3 T. (i) Data from two samples showing skyrmion densities in step 8 ($\boldsymbol{B}_{\parallel} = 0$ T, $\boldsymbol{B}_{\perp} = 0.2/0.3$ T for samples 1 and 2, respectively) manipulated by $\boldsymbol{B}_{\parallel}^*$. (j) Histograms summarizing skyrmion spacing distributions in step 8 ($\boldsymbol{B}_{\perp} = 0.2$ T, $\boldsymbol{B}_{\parallel} = 0$ T) with various $\boldsymbol{B}_{\parallel}^*$. The color-coded manipulation, specific steps, and magnetic-field conditions $[\boldsymbol{B}_{\perp}, \boldsymbol{B}_{\parallel}]$ for each image are indicated in (b), (c), (g), and (h). The shadow areas indicate the trend of the relationships in (d), (e), (i), and (j).

(step 4) exhibit distinct ordering as $\boldsymbol{B}_{\parallel}{}'$ increases, with stripes aligning in the same direction, bending and branching structures disappearing, and more uniform stripe spacing developing across the different values of $\boldsymbol{B}_{\parallel}{}'$ [Fig. 3(b)]. The skyrmion chains in the STA structure (step 8) display similar features to the stripes in step 4, reflecting the strong influence of the in-plane magnetic field $\boldsymbol{B}_{\parallel}{}'$ applied in step 3 [Fig. 3(c)]. The complete procedures for these magnetic-field operations are detailed in the MFM images in Supplemental Material Fig. S10 [36].

The impact of $\boldsymbol{B}_{\parallel}{}'$ on stripe ordering and STA is quantified by statistical analysis of the magnetic structure. The order factors of stripe domains in step 4 ($\boldsymbol{B}_{\perp} = 0.2$ T) are estimated using the aspect ratios R_{I} and R_{S} derived from the quotient of the maximum and minimum values of the integrated intensity curves (extracted from I_{FFT}, red dots) and the shape parameter curves (extracted from S_{FFT}, blue dots). Both methods reveal a strong positive correlation between stripe ordering and varying $\boldsymbol{B}_{\parallel}{}'$ [Fig. 3(d)]). The order factors rise gradually with increasing $\boldsymbol{B}_{\parallel}{}'$, but show slower growth and increased fluctuations when $\boldsymbol{B}_{\parallel}{}'$ exceeds 0.4 T, corresponding to the disappearance of the bending and branching structure [Fig. 3(b)]. As expected, the final density of stripe domains at $\boldsymbol{B}_{\perp} = 0$ T (step 5) increases with $\boldsymbol{B}_{\parallel}{}'$ and is saturated when $\boldsymbol{B}_{\parallel}{}'$ exceeds 0.4 T [Fig. 3(e), blue squares]. However, the density of skyrmions exhibits a nonmonotonic relationship with unexpected parabolic trend, peaking between 0.4 and 0.6 T [Fig. 3(e), red hexagonal stars]. For $\boldsymbol{B}_{\parallel}{}' < 0.4$ T, curled stripes squeeze the space available for skyrmions, while for $\boldsymbol{B}_{\parallel}{}' > 0.4$ T, fine branches rather than skyrmions are observed. Both conditions lead to decreased skyrmion density.

In addition to $\boldsymbol{B}_{\parallel}{}'$, the parameter $\boldsymbol{B}_{\parallel}{}^{*}$ applied to induce precursors of skyrmions (step 6) is critical for controlling skyrmion density. We performed a series of independent vector-magnetic-field operations with various $\boldsymbol{B}_{\parallel}{}^{*}$, specifically $\boldsymbol{B}_{\parallel}{}^{*} = 0.4$, 1, 2, and 3 T [Fig. 3(f)]. MFM images of ultimate STA structures (step 8) reveal a rise of skyrmion density as $\boldsymbol{B}_{\parallel}{}^{*}$ increases [Fig. 3(g)]. To further understand the influence of $\boldsymbol{B}_{\parallel}{}^{*}$ after the formation of aligned stripes, we studied the magnetic structure during $\boldsymbol{B}_{\parallel}{}^{*}$ application (from step 5 to step 6) [Fig. 3(h)]. Gradually increasing $\boldsymbol{B}_{\parallel}{}^{*}$ from 0.4 to 3 T reveals many small branching structures emerging from the stripe domains, which then become spatially separated and lay the groundwork for the skyrmions in STA by providing the initial magnetic topology [37].

The regulation of skyrmion density by $\boldsymbol{B}_{\parallel}{}^{*}$ is further quantified by statistical analysis under various $\boldsymbol{B}_{\parallel}{}^{*}$ values on two samples, demonstrating a strong positive relationship in both samples [Fig. 3(i)]. It is important to note that, the stripe density is not affected by $\boldsymbol{B}_{\parallel}{}^{*}$, but rather sets an upper limit on the number of skyrmion chains sandwiched between the stripes. Consequently, the increasing skyrmion density is primarily due to the reduced spacing among skyrmions within each chain. As expected, histograms summarizing skyrmion spacing reveal a negative relationship with $\boldsymbol{B}_{\parallel}{}^{*}$ [Fig. 3(j)], with spacing at $\boldsymbol{B}_{\parallel}{}^{*} = 0.4$ T being notably larger compared to other values.

IV. TWO TYPES OF SKYRMIONS AND MECHANISMS OF STA GENERATION

Focusing on the behavior of skyrmions in STA (step 8), we compare the generation process of skyrmions under different in-plane magnetic fields, specifically $\boldsymbol{B}_{\parallel}{}^{*} = 0.4$, 1, and 3 T, using MFM measurements in the stripe phase (step 5) and STA phase (step 8) [Fig. 4(a)]. The independent vector-magnetic-field manipulation procedures reveal the evolution paths of two distinct types of skyrmions [Fig. 4(b)]: Skyrmion type I (SkI) generated at lower $\boldsymbol{B}_{\parallel}{}^{*}$ values and skyrmion type II (SkII) generated at higher $\boldsymbol{B}_{\parallel}{}^{*}$ values. The procedure with $\boldsymbol{B}_{\parallel}{}^{*} = 0.4$ T generates SkI, where skyrmions arise from the breakdown of stripe domains (cyan boxes). The transformation from stripe domains to skyrmions typically occurs in thin stripes or weaker parts of stripe domains, which are more fragile under increasing $\boldsymbol{B}_{\perp}$, and are transformed into skyrmion chains preferentially. The procedure with $\boldsymbol{B}_{\parallel}{}^{*} = 3$ T generates SkII (purple boxes), where skyrmions originate from newly formed small branching magnetic structures sandwiched between stripe domains as previously discussed [Fig. 3(h)], resulting in higher skyrmion density. The procedure with $\boldsymbol{B}_{\parallel}{}^{*} = 1$ T generates both types of skyrmions. The observed skyrmion types offer a consistent understanding with the sudden change skyrmion spacing with varying $\boldsymbol{B}_{\parallel}{}^{*}$ [Fig. 3(j)].

The 3D image [Fig. 4(c)] and line profiles [Fig. 4(d)] provide a comparative overview of the two skyrmion types, highlighting differences in the Δf signal strength, skyrmion size, and spacing within skyrmion chains. The distribution of the MFM signal Δf_{sk} (Δf contrast around a single skyrmion) of two types of skyrmions shows that SkI exhibits a significantly higher Δf_{sk} signal (97.7 Hz) compared to SkII (60.5 Hz), indicating stronger out-of-plane magnetization [Fig. 4(e)]. Additionally, extracted full width at half maximum (FWHM) [Fig. 4(f)] reveals a larger size of SkI (1.35 μm) compared to SkII (0.84 μm). The separation within skyrmion chains shows a spacing of around 2.49 μm for SkI, larger than 1.70 μm for SkII [Fig. 4(g)], consistent with the higher skyrmion density for SkII and the decreasing spacing for larger $\boldsymbol{B}_{\parallel}{}^{*}$. These differences suggest distinct three-dimensional magnetic structures for SkI and SkII.

We further investigated the evolution of SkI and SkII with increasing the out-of-plane magnetic field $\boldsymbol{B}_{\perp}$ during step 8. Increasing $\boldsymbol{B}_{\perp}$ from 0.05 to 0.4 T causes the Δf_{sk} of SkI to drop to about one third of its original value, while SkII remains relatively constant, leading to close values

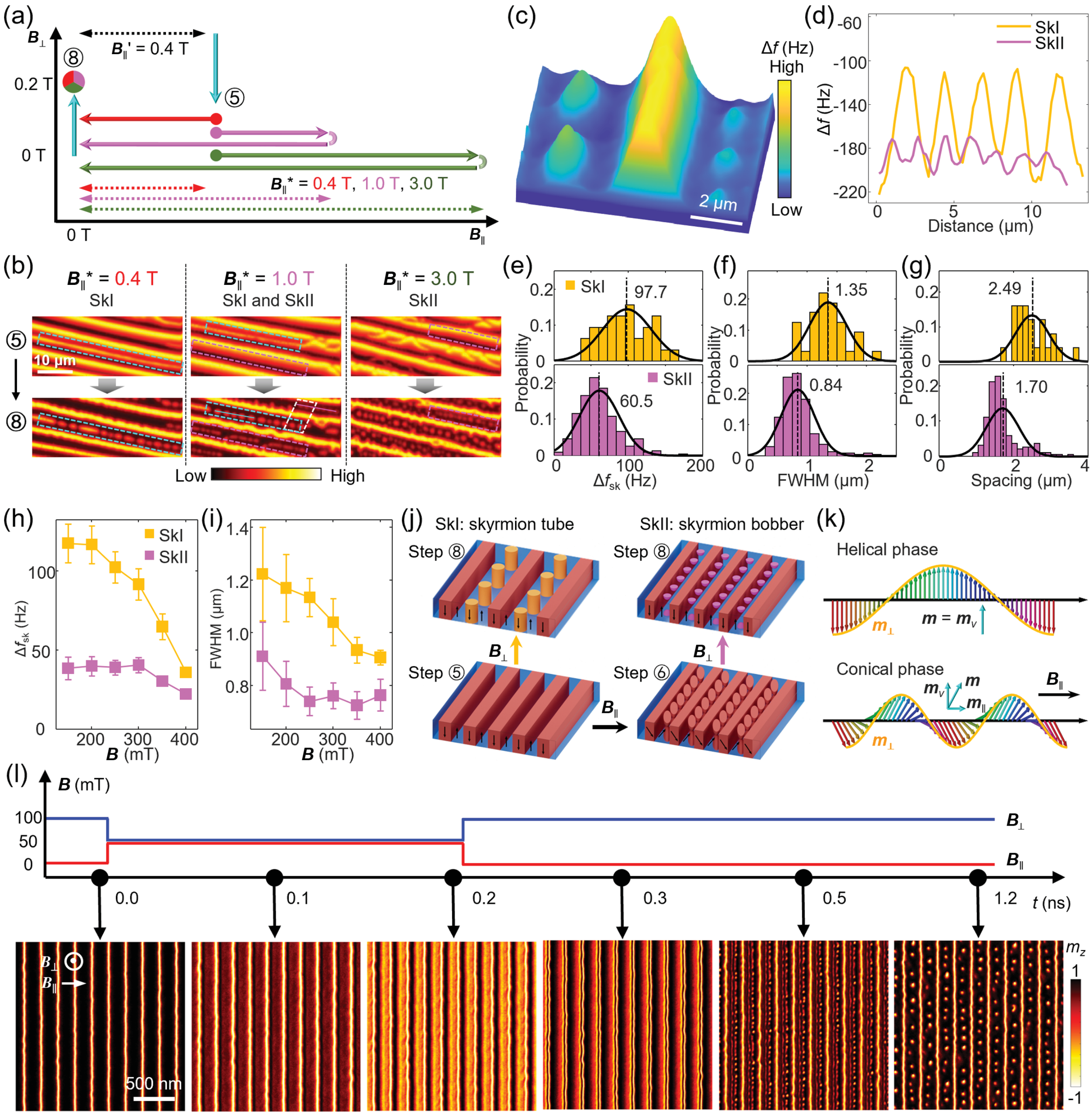

FIG. 4. Coexistence of the two types of skyrmions and mechanism of generation of STA. (a) Schematics of the generation process of STA under different $\boldsymbol{B}_{\parallel}^{*}$. (b) Magnetic domains in step 5 ($\boldsymbol{B}_{\perp} = 0$ T, $\boldsymbol{B}_{\parallel} = 0.4$ T) and step 8 ($\boldsymbol{B}_{\perp} = 0.2$ T, $\boldsymbol{B}_{\parallel} = 0$ T) induced by different $\boldsymbol{B}_{\parallel}^{*}$ in (a), revealing two distinct skyrmion formation mechanisms. (c) Three-dimensional Δf signal map in the white dashed box in (b). (d) Linecuts revealing Δf_{sk} contrast between type-I skyrmions (SkI, orange line) and type-II skyrmions (SkII, purple line) marked by cyan and purple dashed lines in (b), respectively. (e)–(g) Δf_{sk}, FWHM, and spacing distribution of two types of skyrmions in step 8 ($\boldsymbol{B}_{\perp} = 0.2$ T, $\boldsymbol{B}_{\parallel} = 0$ T). (h),(i) Averaged Δf_{sk} and FWHM of two types of skyrmions under increasing $\boldsymbol{B}_{\perp}$ ($\boldsymbol{B}_{\parallel} = 0$ T). (j) Schematics of magnetic domain evolution for two types of skyrmion generation mechanisms. (k) Side view (x-z plane) diagram of magnetic moment distribution in the helical phase and conical phase under in-plane magnetic field $\boldsymbol{B}_{\parallel}$ (x direction). $\boldsymbol{m}_{\mathrm{v}}$ and $\boldsymbol{m}_{\parallel}$ represent the component of magnetic moment $\boldsymbol{m}$ vertical and parallel to the in-plane field direction. $\boldsymbol{m}_{\perp}$ represents the out-of-plane component of $\boldsymbol{m}$. (l) Micromagnetic simulation of the generation process of STA under combined appliance of out-of-plane and in-plane magnetic field.

of both types before vanishing from the measurement at $\boldsymbol{B}_{\perp} = 0.45$ T [see Fig. 4(h) and detailed images in Supplemental Material Fig. S11 [36]]. Additionally, the FWHM of SkI decreases more significantly compared to SkII, approaching a close level at $\boldsymbol{B}_{\perp} = 0.4$ T [Fig. 4(i)].

It is worth noting that, the stronger $\Delta f_{\rm sk}$ of SkI indicates a deeper magnetized structure extending along the z direction, typically the entire sample [10]. In contrast, the weaker $\Delta f_{\rm sk}$ of SkII suggests a surface-localized magnetic structure. Moreover, the shrinking core area of SkI under increasing $\boldsymbol{B}_{\perp}$ reflects a bubblelike structure in the x-y plane [38,39], whereas SkII maintains a nearly consistent size, indicating a pure skyrmion state. A previous theoretical study proposed a chiral bobber model of the skyrmion, which exists at the surface of the sample and aligns with the SkII observed in this work [40]. Subsequent experimental studies have reported the coexistence of skyrmionic bobbers and skyrmionic tubes using multiple techniques [41,42]. More recently, skyrmionic bobbers have been identified and distinguished from skyrmionic tubes based on MFM signal contrast [43,44]. Building on these prior reports and the strong experimental signatures observed in this study, we propose that SkI corresponds to a skyrmionic tube structure, while SkII corresponds to a skyrmionic bobber. A more detailed discussion of three-dimensional structures of skyrmions under in-plane magnetic field is included in Supplementary Material [36].

V. DISCUSSION AND SIMULATION

Our findings highlight the critical role of a strong in-plane magnetic field $\boldsymbol{B}_{\parallel}{}^{*}$ in generating small branching structures and following high-density SkII skyrmions, whereas a lack of strong $\boldsymbol{B}_{\parallel}{}^{*}$ results in SkI skyrmion generation [Fig. 4(j)]. The understanding of $\boldsymbol{B}_{\parallel}{}^{*}$-dependent phenomena begins with the Bloch-type domain wall in Fe_3GaTe_2 bulk, confirmed by the mutually perpendicular relationship between the stripe domains and $\boldsymbol{B}_{\parallel}{}'$ (step 5). The Bloch-type chirality is protected and restricted by bulk DMI [45] defined as $H_{\rm DMI} = -\boldsymbol{D}_{\rm ij} \cdot (\boldsymbol{m}_i \times \boldsymbol{m}_j)$, which allows $\boldsymbol{B}_{\parallel}$ to modulate the propagation period of stripe domains and consequently squeezing out sandwiched small branching structures and following skyrmion chains from the stripe domains.

The applied $\boldsymbol{B}_{\parallel}$ introduces a parallel component $\boldsymbol{m}_{\parallel}$ to the magnetic moment $\boldsymbol{m}$, resulting in the transition of Fe_3GaTe_2 bulk magnetic structure from a helical phase to a conical phase [Fig. 4(k)] [2]. Under a strong in-plane magnetic field $\boldsymbol{B}_{\parallel}{}^{*}$ along the x direction, the system's original vertical magnetic moment $\boldsymbol{m}$ tilts toward the field direction, reducing its vertical component $\boldsymbol{m}_{\rm v}$ in the y-z plane [46,47]. In steady-state conditions, the rotation of $\boldsymbol{m}_{\rm v}$ perpendicular to $\boldsymbol{B}_{\parallel}$ provides a nonzero cross-product term $(\boldsymbol{m}_{\rm vi} \times \boldsymbol{m}_{\rm vj})$ for DMI energy. As the magnitude of $\boldsymbol{m}_{\rm v}$ decreases, maintaining consistent DMI energy requires $\boldsymbol{m}_{\rm v}$ to rotate with a higher angular velocity in space, resulting in a shorter propagation period of stripe domains. When $\boldsymbol{B}_{\parallel}{}^{*}$ becomes sufficiently strong to double the angular velocity of $\boldsymbol{m}_{\rm v}$, new magnetic domains emerge between the two existing stripes. The formation mechanisms are strongly supported by the experimental measurements of $\boldsymbol{B}_{\parallel}$-dependent $\boldsymbol{m}_{\perp}$ variations [Fig. 3(h)].

Subsequently, in step 7, as $\boldsymbol{B}_{\parallel}$ is reduced to zero, the in-plane component of $\boldsymbol{m}$ vanishes, driving the system from the conical phase back to the helical phase, while the newly formed fractional magnetic domains persist due to topological protection. Finally, with the increase of $\boldsymbol{B}_{\perp}$ in step 8, magnetic domains with inverse $\boldsymbol{m}_{\perp}$ are eroded, thereby transforming the fractional magnetic domains into skyrmion chains.

We further confirmed the formation mechanism of STA by performing micromagnetic simulations based on the Landau-Lifshitz-Gilbert equation, considering multiple factors including the Zeeman effect, magnetocrystalline anisotropy, Heisenberg exchange, DMI, demagnetization, and finite temperature.

The initial state of the simulation is set as highly oriented stripe domains with an out-of-plane magnetic field $\boldsymbol{B}_{\perp}$ [Fig. 4(l)] corresponding to the stripe phase observed experimentally in steps 4 and 5. When applying an in-plane magnetic field $\boldsymbol{B}_{\parallel}$, additional signals gradually emerge, showing less prominent stripe patterns between the initial stripes due to the shortened propagation period, corresponding to experimental patterns in step 6. Simulating the magnetic operation in steps 7 and 8 by withdrawing the in-plane magnetic field and restoring the out-of-plane magnetic field successfully restores both the propagation period and the initial stripe pattern. The less prominent stripe patterns gradually transform into fragmental structures and finally into skyrmion chains between the initial stripes, reproducing the highly oriented STA structure in the simulation. Furthermore, micromagnetic simulations confirmed the Bloch-type nature of skyrmions in STA, consistent with the Bloch-type domain-wall behavior observed in stripe domains [Figs. S7(d)–S7(e) in Supplemental Material [36]]. The full evolution process of magnetic domains in simulation is shown in detail in Supplemental Material Video S2 [36].

A careful analysis of the experimental results and simulations reveals several key magnetic properties of Fe_3GaTe_2 that play a role in the formation of STA, including DMI, anisotropy, and demagnetizing energy. External factors, such as the temperature, also exert an influence. We propose that by deliberately controlling these factors, STA could be extended to a broader range of magnetic materials and spintronic devices (see Supplemental Material "Generalization of STA" and "Temperature dependence of STA formation" [36]).

In conclusion, we reported the generation of a large-area, highly oriented STA in ferromagnet Fe_3GaTe_2. The orientation and ordering of STA, as well as the density and types of skyrmions, are all efficiently manipulated by our strategy with vector-magnetic-field operations. We examined the behavioral differences and formation processes of two distinct skyrmion types, finding that the unique formation mechanism of type-II skyrmions in STA is closely tied to the interplay between DMI and the in-plane magnetic field, as supported by simulation results. This approach for generating ordered magnetic structures with high skyrmion density holds promising potential for application in skyrmion-based spintronic devices, where straight stripe domains may serve as racetracks to confine current-driven skyrmion motions in further attempts.

ACKNOWLEDGMENTS

This work is supported by grants from the National Natural Science Foundation of China (Grants No. 62488201 and No. 12374199), the National Key Research and Development Projects of China (Grant No. 2022YFA1204100), the Beijing Nova Program (Grant No. 20240484651),and the Innovation Program of Quantum Science and Technology (Grant No. 2021ZD0302700).

[1] A. Fert, V. Cros, and J. Sampaio, *Skyrmions on the track*, Nat. Nanotechnol. **8**, 152 (2013).

[2] S. Mühlbauer, B. Binz, F. Jonietz, C. Pfleiderer, A. Rosch, A. Neubauer, R. Georgii, and P. Böni, *Skyrmion lattice in a chiral magnet*, Science **323**, 915 (2009).

[3] X. Z. Yu, Y. Onose, N. Kanazawa, J. H. Park, J. H. Han, Y. Matsui, N. Nagaosa, and Y. Tokura, *Real-space observation of a two-dimensional skyrmion crystal*, Nature (London) **465**, 901 (2010).

[4] S. Seki, X. Z. Yu, S. Ishiwata, and Y. Tokura, *Observation of skyrmions in a multiferroic material*, Science **336**, 198 (2012).

[5] T. Kurumaji, T. Nakajima, M. Hirschberger, A. Kikkawa, Y. Yamasaki, H. Sagayama, H. Nakao, Y. Taguchi, T. Arima, and Y. Tokura, *Skyrmion lattice with a giant topological Hall effect in a frustrated triangular-lattice magnet*, Science **365**, 914 (2019).

[6] L. Powalla *et al.*, *Seeding and emergence of composite skyrmions in a van der Waals magnet*, Adv. Mater. **35**, 2208930 (2023).

[7] W. Jiang *et al.*, *Blowing magnetic skyrmion bubbles*, Science **349**, 283 (2015).

[8] V. T. Pham *et al.*, *Fast current-induced skyrmion motion in synthetic antiferromagnets*, Science **384**, 307 (2024).

[9] A. Soumyanarayanan *et al.*, *Tunable room-temperature magnetic skyrmions in* Ir/Fe/Co/Pt *multilayers*, Nat. Mater. **16**, 898 (2017).

[10] A.-O. Mandru, O. Yıldırım, R. Tomasello, P. Heistracher, M. Penedo, A. Giordano, D. Suess, G. Finocchio, and H. J. Hug, *Coexistence of distinct skyrmion phases observed in hybrid ferromagnetic/ferrimagnetic multilayers*, Nat. Commun. **11**, 6365 (2020).

[11] H. Du, J. P. DeGrave, F. Xue, D. Liang, W. Ning, J. Yang, M. Tian, Y. Zhang, and S. Jin, *Highly stable skyrmion state in helimagnetic* MnSi *nanowires*, Nano Lett. **14**, 2026 (2014).

[12] N. Mathur, F. S. Yasin, M. J. Stolt, T. Nagai, K. Kimoto, H. Du, M. Tian, Y. Tokura, X. Yu, and S. Jin, *In-plane magnetic field-driven creation and annihilation of magnetic skyrmion strings in nanostructures*, Adv. Funct. Mater. **31**, 2008521 (2021).

[13] C. Gong *et al.*, *Discovery of intrinsic ferromagnetism in two-dimensional van der Waals crystals*, Nature (London) **546**, 265 (2017).

[14] B. Huang *et al.*, *Layer-dependent ferromagnetism in a van der Waals crystal down to the monolayer limit*, Nature (London) **546**, 270 (2017).

[15] G. Zhang, F. Guo, H. Wu, X. Wen, L. Yang, W. Jin, W. Zhang, and H. Chang, *Above-room-temperature strong intrinsic ferromagnetism in 2D van der Waals* Fe_3GaTe_2 *with large perpendicular magnetic anisotropy*, Nat. Commun. **13**, 5067 (2022).

[16] W. Li *et al.*, *Room-temperature van der Waals ferromagnet switching by spin-orbit torques*, Adv. Mater. **35**, 2303688 (2023).

[17] Y. Ji *et al.*, *Direct observation of room-temperature magnetic skyrmion motion driven by ultra-low current density in van der Waals ferromagnets*, Adv. Mater. **36**, 2312013 (2024).

[18] Z. Li *et al.*, *Room-temperature sub-100 nm Néel-type skyrmions in non-stoichiometric van der Waals ferromagnet* $Fe_{3-x}GaTe_2$ *with ultrafast laser writability*, Nat. Commun. **15**, 1017 (2024).

[19] C. Zhang *et al.*, *Above-room-temperature chiral skyrmion lattice and Dzyaloshinskii-Moriya interaction in a van der Waals ferromagnet* $Fe_{3-x}GaTe_2$, Nat. Commun. **15**, 4472 (2024).

[20] H. Zhang *et al.*, *Spin disorder control of topological spin texture*, Nat. Commun. **15**, 3828 (2024).

[21] X. Lv *et al.*, *Distinct skyrmion phases at room temperature in two-dimensional ferromagnet* Fe_3GaTe_2, Nat. Commun. **15**, 3278 (2024).

[22] G. Hu *et al.*, *Room-temperature antisymmetric magnetoresistance in van der Waals ferromagnet* Fe_3GaTe_2 *nanosheets*, Adv. Mater. **36**, 2403154 (2024).

[23] H. Shi *et al.*, *Dynamic behavior of above-room-temperature robust skyrmions in 2D van der Waals magnet*, Nano Lett. **24**, 11246 (2024).

[24] S. Woo *et al.*, *Observation of room-temperature magnetic skyrmions and their current-driven dynamics in ultrathin metallic ferromagnets*, Nat. Mater. **15**, 501 (2016).

[25] H. Zhang *et al.*, *Room-temperature skyrmion lattice in a layered magnet* $(Fe_{0.5}Co_{0.5})_5GeTe_2$, Sci. Adv. **8**, eabm7103 (2022).

[26] S.-G. Je *et al.*, *Creation of magnetic skyrmion bubble lattices by ultrafast laser in ultrathin films*, Nano Lett. **18**, 7362 (2018).

[27] Y. Guang *et al.*, *Creating zero-field skyrmions in exchange-biased multilayers through x-ray illumination*, Nat. Commun. **11**, 949 (2020).

[28] Y. Guang *et al.*, *Electron beam lithography of magnetic skyrmions*, Adv. Mater. **32**, 2003003 (2020).

[29] Z. Li *et al.*, *Electron-assisted generation and straight movement of skyrmion bubble in kagome* $TbMn_6Sn_6$, Adv. Mater. **36**, 2309538 (2024).

[30] N. Romming, C. Hanneken, M. Menzel, J. E. Bickel, B. Wolter, K. Von Bergmann, A. Kubetzka, and R. Wiesendanger, *Writing and deleting single magnetic skyrmions*, Science **341**, 636 (2013).

[31] W. Jiang *et al.*, *Direct observation of the skyrmion Hall effect*, Nat. Phys. **13**, 162 (2017).

[32] G. Yu *et al.*, *Room-temperature skyrmion shift device for memory application*, Nano Lett. **17**, 261 (2017).

[33] C. Song, L. Zhao, J. Liu, and W. Jiang, *Experimental realization of a skyrmion circulator*, Nano Lett. **22**, 9638 (2022).

[34] Z. He *et al.*, *Experimental observation of current-driven antiskyrmion sliding in stripe domains*, Nat. Mater. **23**, 1048 (2024).

[35] Z. Li *et al.*, *Field-free topological behavior in the magnetic domain wall of ferrimagnetic* GdFeCo, Nat. Commun. **12**, 5604 (2021).

[36] Supplemental Material at http://link.aps.org/supplemental/10.1103/PhysRevX.15.021032 for more details of methods, analysis and extended data.

[37] H. Du *et al.*, *Edge-mediated skyrmion chain and its collective dynamics in a confined geometry*, Nat. Commun. **6**, 8504 (2015).

[38] X. Yu, M. Mostovoy, Y. Tokunaga, W. Zhang, K. Kimoto, Y. Matsui, Y. Kaneko, N. Nagaosa, and Y. Tokura, *Magnetic stripes and skyrmions with helicity reversals*, Proc. Natl. Acad. Sci. U.S.A. **109**, 8856 (2012).

[39] M.-G. Han, J. A. Garlow, Y. Liu, H. Zhang, J. Li, D. DiMarzio, M. W. Knight, C. Petrovic, D. Jariwala, and Y. Zhu, *Topological magnetic-spin textures in two-dimensional van der Waals* $Cr_2Ge_2Te_6$, Nano Lett. **19**, 7859 (2019).

[40] F. N. Rybakov, A. B. Borisov, S. Blügel, and N. S. Kiselev, *New type of stable particlelike states in chiral magnets*, Phys. Rev. Lett. **115**, 117201 (2015).

[41] F. Zheng *et al.*, *Experimental observation of chiral magnetic bobbers in B20-type* FeGe, Nat. Nanotechnol. **13**, 451 (2018).

[42] K. Ran, Y. Liu, Y. Guang, D. M. Burn, G. van der Laan, T. Hesjedal, H. Du, G. Yu, and S. Zhang, *Creation of a chiral bobber lattice in helimagnet-multilayer heterostructures*, Phys. Rev. Lett. **126**, 017204 (2021).

[43] M. Grelier, F. Godel, A. Vecchiola, S. Collin, K. Bouzehouane, A. Fert, V. Cros, and N. Reyren, *Three-dimensional skyrmionic cocoons in magnetic multilayers*, Nat. Commun. **13**, 6843 (2022).

[44] A. K. Gopi, A. K. Srivastava, A. K. Sharma, A. Chakraborty, S. Das, H. Deniz, A. Ernst, B. K. Hazra, H. L. Meyerheim, and S. S. P. Parkin, *Thickness-tunable zoology of magnetic spin textures observed in* Fe_5GeTe_2, ACS Nano **18**, 5535 (2024).

[45] A. Chakraborty *et al.*, *Magnetic skyrmions in a thickness tunable 2D ferromagnet from a defect driven Dzyaloshinskii-Moriya interaction*, Adv. Mater. **34**, 2108637 (2022).

[46] J. Masell, X. Yu, N. Kanazawa, Y. Tokura, and N. Nagaosa, *Combing the helical phase of chiral magnets with electric currents*, Phys. Rev. B **102**, 180402(R) (2020).

[47] V. Ukleev, Y. Yamasaki, O. Utesov, K. Shibata, N. Kanazawa, N. Jaouen, H. Nakao, Y. Tokura, and T. H. Arima, *Metastable solitonic states in the strained itinerant helimagnet* FeGe, Phys. Rev. B **102**, 014416 (2020).